JOURNAL OF GEOPHYSICAL RESEARCH, VOL. ???, XXXX, DOI:10.1029/,

Mixing and dissipation in a geostrophic buoyancy-driven circulation

Catherine A. Vreugdenhil,[1] Bishakhdatta Gayen,[1] Ross W. Griffiths[1]

Key points:

1. Energy budget is fully resolved in a turbulent geostrophic circulation driven by buoyancy forcing

2. Turbulent mixing and heat transport are reduced by planetary rotation, viscous dissipation remains unchanged

3. Energy from surface buoyancy forcing mostly goes to mixing rather than viscous dissipation

Catherine A. Vreugdenhil, Research School of Earth Sciences, Australian National University, Canberra, ACT 2601, Australia. (Catherine.Vreugdenhil@anu.edu.au)

[1]Research School of Earth Sciences,
Australian National University, Canberra,
Australia.

Abstract.

Turbulent mixing and energy dissipation have important roles in the global circulation but are not resolved by ocean models. We use direct numerical simulations of a geostrophic circulation, resolving turbulence and convection, to examine the rates of dissipation and mixing. As a starting point, we focus on circulation in a rotating rectangular basin forced by a surface temperature difference but no wind stress. Emphasis is on the geostrophic regime for the horizontal circulation, but also on the case of strong buoyancy forcing (large Rayleigh number), which implies a turbulent convective boundary layer. The computed results are consistent with existing scaling theory that predicts dynamics and heat transport dependent on the relative thicknesses of thermal and Ekman boundary layers, hence on the relative roles of buoyancy and rotation. Scaling theory is extended to describe the volume-integrated rate of mixing, which is proportional to heat transport and decreases with increasing rotation rate or decreasing temperature difference. In contrast, viscous dissipation depends crucially on whether the thermal boundary layer is laminar or turbulent, with no direct Coriolis effect on the turbulence unless rotation is extremely strong. For strong forcing, in the geostrophic regime, the mechanical energy input from buoyancy goes primarily into mixing rather than dissipation. For a buoyancy-driven circulation in a basin comparable to the North Atlantic we estimate that the total rate of mixing accounts for over 95% of the mechanical energy supply, implying that buoyancy is an efficient driver of mixing in the oceans.

1. Introduction

The mechanical energy budget of the ocean is a governor for the dynamics of the global circulation [*Ferrari and Wunsch*, 2009; *Marshall and Speer*, 2012]. There are two energy sinks in the budget: viscous dissipation (predominantly in turbulence) removes kinetic energy and irreversible mixing of the density field is a sink of available potential energy [*Hughes et al.*, 2009; *Nikurashin and Ferrari*, 2011; *Nikurashin et al.*, 2013]. Mixing converts available potential energy into background potential energy that is no longer available to drive motion [*Winters et al.*, 1995]. Kinetic energy is produced by wind stress and tides, and by conversion of available potential energy to motion, notably in internal waves, baroclinic instability and convection. The available potential energy is generated by surface buoyancy forcing (and effects of the non-linear equation of state). In steady state and neglecting geothermal fluxes, the rate of energy going to mixing must match the rate of generation of available potential energy by surface buoyancy forcing [*Hughes et al.*, 2009; *Tailleux*, 2009]. This statement holds irrespective of the cause of the mixing, whether it be wind stress, tides, convection or any other source of mechanical energy. However, global ocean models do not close the mechanical energy budget, instead they use a local diapycnal mixing rate that is either prescribed or based on an empirical parameterisation, and do not explicitly consider the dissipation of energy.

The conversion of available to background potential energy by irreversible mixing relative to the total mechanical energy supply, referred to as the mixing efficiency [*Peltier and Caulfield*, 2003], has implications for the total amount of mixing in the oceans. It also has implications for the relative importance of surface buoyancy forcing to other energy inputs such as winds and tides, and for the amount of dissipation that must be achieved by a range of mechanisms. Some studies have downplayed the importance of surface buoyancy forcing [*Wunsch and Ferrari*, 2004; *Kuhlbrodt et al.*, 2007; *Nycander et al.*, 2007], whereas others find evidence that the mechanical power input to the oceans from surface buoyancy forcing is comparable with that from wind stress [*Saenz et al.*, 2012; *Zemskova et al.*, 2015] or show that key components of the global circulation involve a substantial influence of buoyancy [*Morrison et al.*, 2011, 2015]. Other studies have addressed additional mechanisms that can direct energy, particularly from geostrophic flow, to small scale turbulent dissipation [*Dewar et al.*, 2011], but it is not clear how much turbulent dissipation is required to balance a given energy input.

The strong tie between mixing rate and surface buoyancy forcing, coupled with the knowledge that differential surface buoyancy fluxes are a necessity for maintaining a stratified ocean, means that a purely buoyancy forced flow is the obvious case with which to begin an examination of the fully resolved mechanical energy budget of geostrophic circulation. Wind and other energy sources will generally influence the surface buoyancy forcing through a variety of complex coupling mechanisms worthy of further investigation [*Saenz et al.*, 2012], as well as introducing additional kinetic energy and the consequent viscous dissipation. However, this does not alter the fact that the domain integrated rate of mixing must equal the rate of available potential energy input. The buoyancy forced case also allows unambiguous identification of the energy pathway from buoyancy forcing to viscous dissipation.

Scaling theory for flow with laminar boundary layers indicates that the dynamics of a rotating, buoyancy-driven circulation is dependent on the ratio of the thermal and Ekman frictional boundary layer thicknesses adjacent to the forcing boundary, as shown in a cylinder with a radial temperature gradient on a horizontal surface [*Hignett et al.*, 1981]. The importance of the ratio of boundary layer thicknesses for the transition from non-rotating to strong rotational effects has also been shown for turbulent Rayleigh-Bénard convection [*King et al.*, 2009]. In both cases, when rotation is weak, the thermal boundary layer lies well within the Ekman layer and rotational effects in the thermal boundary layer are secondary to the non-rotating momentum balance, which for small Rayleigh numbers (where the laboratory Rayleigh number is a measure of the magnitude of the buoyancy forcing along the domain length to diffusion and viscous effects at a molecular level) reduces to the viscous-buoyancy balance [*Rossby*, 1965]. The heat transport remains largely unaffected by the Coriolis control on flow in the bulk of the domain outside the Ekman layer. With rapid rotation, frictional effects are confined to an Ekman layer much thinner than the thermal boundary layer. The largest scales of horizontal motion in the thermal boundary layer are influenced by rotation and are governed by an inviscid geostrophic balance, as proposed in many scaling analyses for the basin scale of ocean circulation [*Robinson and Stommel*, 1959; *Robinson*, 1960; *Bryan*, 1987; *Winton*, 1996; *Park and Bryan*, 2000]. The geostrophic constraint on flow reduces advection of heat in the direction of the applied temperature gradient, thickens the thermal boundary layer and decreases the vertical temperature gradient at the boundary.

The scaling theory for the geostrophic regime is consistent with general circulation models [*Winton*, 1996; *Park and Bryan*, 2000], as well as with laboratory experiments in a rectangular basin with differential heating (as an imposed flux) and cooling (as an applied temperature) along the base at Rayleigh number $Ra \approx 10^{11}$ [*Park and Whitehead*, 1999].

Given the presence of meridional sidewalls (parallel to the applied temperature gradient) heat transport is achieved by baroclinic eddies and boundary currents. In addition a regime transition from viscous to inertial scaling has been shown to occur in direct numerical simulations of the non-rotating case at $Ra > 10^{11}$ [*Gayen et al.*, 2014]. In the inertial regime small-scale three-dimensional convection and shear instabilities develop a convective mixed layer adjacent to the destabilising boundary flux and within the thermal boundary layer, and come to dominate the heat transport [*Mullarney et al.*, 2004]. The scaling analysis for rotating flow has not been tested in the context of a turbulent thermal boundary layer.

In the absence of Coriolis effects and wind stress a buoyancy-driven overturning circulation forced by a surface temperature gradient (non-rotating horizontal convection) shows a mixing rate much greater than the rate of dissipation of kinetic energy at large Rayleigh numbers [*Gayen et al.*, 2013, 2014; *Scotti and White*, 2011, 2014]. Scaling theory for this case predicts that the mixing efficiency η (again defined as the conversion rate of mixing as a proportion of the total energy sink, the sum of turbulent dissipation and mixing, *Peltier and Caulfield* [2003]) takes a simple form irrespective of whether the system is rotating [*Gayen et al.*, 2013, 2014]:

$$\eta \approx 1 - A^{-1} Nu^{-1}, \tag{1}$$

where A is the height-to-length basin aspect ratio and Nu, a Nusselt number, is a measure of the convective heat flux compared to a scale for conductive heat flux in the absence of flow. This scaling was confirmed by simulations of non-rotating horizontal convection at $10^{11} < Ra < 10^{15}$ and implies $\eta \to 1$ at large Nu [*Gayen et al.*, 2014]. In this kind of flow the forcing is therefore very efficient at producing mixing, and the amount of energy that must be dissipated by turbulent motions is relatively small. However, the theory has not been tested in the geostrophic regime, particularly at very large Ra for which convective turbulence is expected to be active and to control the heat transport. Although rotation and geostrophy tend to inhibit heat transport, large Nu and high efficiency are again likely to occur at the very large Rayleigh numbers relevant to geophysical conditions. One study has reported a significant reduction of mixing efficiency for circulation in a zonal re-entrant channel model in the presence of rapid rotation, but in the laminar boundary layer regime ($Ra \approx 10^8$) and without resolved Ekman layers [*Barkan et al.*, 2013]. Extrapolation to ocean conditions demands examination of the rotating circulation under turbulent conditions and our purpose here is to fully resolve such a flow. Our hypothesis for the geostrophic regime is that the relatively small-scale turbulence and dissipation remain largely unchanged by Coriolis effects, as does the relationship between the heat transport and mixing efficiency. This leaves mixing as the dominant energy sink accounting for the power input from surface buoyancy forcing and thus heat can be transported through the system with minimal dissipation of kinetic energy.

In §2 we discuss the scaling theory applicable to a set of dynamical regimes, focus on the geostrophic scaling regime and then derive scaling relations for mixing and dissipation. The methodology for direct numerical simulations (DNS) to fully resolve turbulence and dissipation in a buoyancy-driven circulation in a rectangular basin are given in §3. In §4 we discuss the computed results in light of the geostrophic scaling for the thermal boundary layer, heat flux and mechanical energy budget. The scaling relations for mixing, dissipation and mixing efficiency are applied to an idealised ocean basin with realistic thermal forcing and dimensions in §6. Concluding remarks are given in §7.

2. Scaling theory

We consider a rectangular basin of length L, width W and water depth H, with Coriolis parameter f, as shown in Figure 1. The horizontal base has an applied uniform temperature T_c over half of the length and a higher temperature T_h over the other half. This buoyancy forcing is designed to be consistent with past laboratory experiments and numerical studies in non-rotating horizontal convection [*Mullarney et al.*, 2004; *Griffiths et al.*, 2013; *Gayen et al.*, 2014] and is analogous to an upside-down ocean: the vertical coordinates have simply been inverted. The fluid has constant and uniform properties, including viscosity ν, thermal diffusivity κ and expansion coefficient α, specific heat c_p and variable density ρ. The governing parameters are Rayleigh, Ekman and Prandtl numbers, and vertical and horizontal aspect ratios,

$$Ra = \frac{g\alpha\Delta T L^3}{\nu\kappa},\ E = \frac{\nu}{fL^2},\ Pr = \frac{\nu}{\kappa},\ A = \frac{H}{L},\ B = \frac{W}{L}, \tag{2}$$

respectively, where g is gravity and $\Delta T = T_h - T_c$ is the applied temperature difference [*Rossby*, 1965, 1998]. The resulting heat transport is described by the Nusselt number $Nu = FL/(\rho_r c_p \kappa \Delta T)$, where F is the input heat flux per unit area and ρ_r is a reference density.

2.1. Non-rotating scaling

In horizontal convection without rotation ($E^{-1} = 0$) [*Rossby*, 1998; *Mullarney et al.*, 2004; *Gayen et al.*, 2014] a stable thermal boundary layer forms on the cooled region of the base and flows across to the heated region, where it warms and feeds an endwall plume. The circulation is closed by broadly distributed downwelling outside the plume and into the stable boundary layer. In a thermally equilibrated (and time-averaged) state there must be zero net heat flux through every horizontal level of the domain.

Established scaling for the non-rotating case gives thermal boundary layer thickness δ_0, Nusselt number Nu_0 and boundary layer velocity U_0, where the zero subscript specifies the non-rotating case. In the laminar viscous regime [*Rossby*, 1965] these become:

$$\delta_{0\nu} = c_{1\nu} L Ra^{-1/5},\ Nu_{0\nu} = c_{2\nu} Ra^{1/5},$$

$$U_{0\nu} \sim (\kappa/L) Ra^{2/5}, \tag{3}$$

where the subscript ν indicates the viscous regime and the prefactors c_i are evaluated from experiments or simulations ($c_{1\nu} = 2.50$ and $c_{2\nu} = 0.37$; velocity prefactors are omitted because they will not be used here). For the non-rotating inviscid regime, dominated by an inertia-buoyancy balance [*Hughes et al.*, 2007; *Gayen et al.*, 2014], the scaling gives:

$$\delta_0 = c_1 L (RaPr)^{-1/5},\ Nu_0 = c_2 (RaPr)^{1/5},$$

$$U_0 \sim (\kappa/L)(RaPr)^{2/5}, \tag{4}$$

where $c_1 = 3.39$ and $c_2 = 0.37$. The momentum and thermal boundary layers have the same thickness.

The volume-integrated viscous dissipation rate is defined as $\varepsilon = \rho_r \nu \int (\partial u_i/\partial x_j)^2 dV$, where u is the velocity vector, x is the displacement vector, the subscripts i and j are orthogonal directions, V is the volume and summation is implied. In the time-averaged thermally equilibrated state and in the absence of wind stress, ε must equal the rate of production of potential energy from diffusion of heat down the mean vertical temperature gradient, Φ_i [*Paparella and Young*, 2002; *Hughes et al.*, 2009]. DNS for the non-rotating case [*Gayen et al.*, 2013] has confirmed this equality and the scaling

$$\varepsilon_0 = c_3 \rho_r \kappa^3 W Ra Pr/(2L^2), \tag{5}$$

which indicates that the dissipation scales directly with Rayleigh number and hence with the strength of buoyancy forcing. The prefactor c_3 is determined by DNS for each Ra; for large Ra, $c_3 \to 1$. The dissipation in the system is limited to a maximum value ε_{max} given by (5) with $c_3 = 1$ [*Paparella and Young*, 2002]. DNS also shows that this dissipation is overwhelmingly within the boundary layer in the laminar regime, but is increasingly distributed through the depth for increasing Rayleigh number in the turbulent regime [*Gayen et al.*, 2014].

The rate of available potential energy lost to background potential energy by irreversible mixing is $\Phi_d = -g \int_V \kappa (dz^*/d\rho)(\partial\rho/\partial x_i)^2 dV$, where z^* is the height associated with each water parcel if it were adiabatically re-ordered along with all other water parcels, into the rest state of gravitational equilibrium. In a time-averaged flow, Φ_d is equal to the flux of available potential energy due to buoyancy forcing at the boundary and can be written as $\Phi_d = \kappa g \oint z^* (\partial\rho/\partial x_i) dS$, where S is the surface area of the domain [*Tailleux*, 2009; *Hughes et al.*, 2009; *Gayen et al.*, 2013, 2014]. Noting that the buoyancy forcing is only applied at the base, and approximating the surface integral of z^* by a step function which predicts that the water parcels adjacent to the heated region will to rise to $z = H$ while the water parcels at the cooled region remain at $z = 0$, we find the relation $\Phi_d \approx \kappa g H W L/2(\overline{d\rho/dz})$ where $\overline{d\rho/dz}$ is the (spatially averaged) vertical buoyancy gradient applied at the heated boundary. A measure for the Nusselt number is $Nu = (\overline{d\rho/dz})/(\Delta\rho/L)$ which, coupled with the assumption of a linear equation of state $\Delta\rho/\rho_r = \alpha\Delta T$ and the definition of

ε_{max}, gives the scaling

$$\Phi_{d0}/\varepsilon_{max} = c_4 Nu_0 A, \tag{6}$$

where $c_4 = 0.89$ for the laminar viscous regime and $c_4 = 0.68$ for the inviscid regime [*Gayen et al.*, 2014]. This relation holds in both the viscous and inviscid cases and, along with (3) and (4), shows that the mixing rate increases with the strength of buoyancy forcing.

The mixing efficiency η for the steady state surface buoyancy-forced circulation, where $\Phi_i = \varepsilon$, can be written as

$$\eta = \frac{\Phi_d - \Phi_i}{\Phi_d - \Phi_i + \varepsilon} = 1 - \varepsilon/\Phi_d, \tag{7}$$

regardless of the presence or absence of rotation [*Hughes et al.*, 2009; *Gayen et al.*, 2013]. The relation (7) reduces to (1) on assuming that the dissipation approaches the maximum dissipation limit ($\varepsilon \approx \varepsilon_{max}$), which is the case in non-rotating DNS for the inviscid regime, and applying (6) without the prefactor. The relation (1) has been shown to agree with non-rotating DNS for $Ra > 10^{11}$ [*Gayen et al.*, 2014].

2.2. Geostrophic scaling

The role of rotation depends on the ratio of the thermal boundary layer thickness to the Ekman layer thickness, $\delta_E = (\nu/f)^{1/2} = LE^{1/2}$. *Hignett et al.* [1981] defined the relevant dimensionless parameter for the laminar case,

$$Q_\nu = Ra^{-2/5} E^{-1}, \tag{8}$$

which is the square of the ratio of boundary layer thicknesses (but using the non-rotating scaling for the thermal boundary layer thickness) and is proportional to the rotation rate. Here we also consider $Q \sim (\delta_0/\delta_E)^2$ for the large Rayleigh number regime and, using the scaling for the non-rotating inviscid thermal boundary layer thickness, we define

$$Q = (RaPr)^{-2/5}E^{-1}. \tag{9}$$

Thus our hypothesis is that one parameter Q is not sufficient to delineate flow regimes, and the Rayleigh number additionally determines whether instabilities modify the dependence on Rayleigh and Prandtl number.

The dynamical regimes identified by *Hignett et al.* [1981] are i) non-rotating ($Q = 0$), ii) very weak rotation ($Q \ll Pr^{-1} \ll 1$), iii) weak rotation ($Pr^{-1} \ll Q \ll 1$), iv) medium rotation ($Q \sim 1$), v) strong rotation ($Q \gg 1$ and $\delta < H$, the geostrophic regime) and vi) extreme rotation ($Q \gg 1$, no thermal boundary layer and conduction dominant). The strong rotation regime (v) is of primary focus here, as this is the geostrophic regime that is expected to be relevant to the ocean (see §6 for further discussion on the ocean application).

In the geostrophic regime a thermal wind balance is assumed for horizontal flow which, along with a balance of vertical advection and diffusion in the thermal boundary layer [*Robinson and Stommel*, 1959; *Robinson*, 1960; *Bryan*, 1987; *Winton*, 1996; *Park and Bryan*, 2000], leads to the scaling

$$\delta \sim L(RaE)^{-1/3},\ Nu \sim (RaE)^{1/3},$$

$$U \sim (\kappa/L)(RaE)^{2/3}. \tag{10}$$

It is useful to normalise these by the inviscid (i.e. inertia-buoyancy dominated) non-rotating scales and express the results in terms of Q to show the significance of the boundary layers. Thus for the turbulent boundary layer regime the geostrophic scaling expected at $Q \gg 1$ becomes (with prefactors to be determined from experiments or DNS):

$$\delta/\delta_0 = c_5 (QPr)^{1/3}, \tag{11}$$

$$Nu/Nu_0 = c_6 (QPr)^{-1/3}. \tag{12}$$

Note that at smaller Ra the laminar flow in the thermal boundary layer transitions (at $Q_\nu = O(1)$) from the viscous non-rotating regime to inviscid (but most probably still laminar) geostrophic flow as rotation is increased. Irrespective of the Rayleigh number, the geostrophic regime is expected to give way to a conductive regime when $\delta \geq H$, which occurs under extremely rapid rotation, hence at $E^{-1} \geq A^3 Ra$. The existence of this conductive regime (which is also referred to as the 'rotation-dominated' regime) has been shown in numerical simulations of rotating horizontal convection in a cylindrical geometry [*Hussam et al.*, 2014; *Sheard et al.*, 2016].

In the geostrophic regime, rotation decouples the Ekman frictional layer from the thermal boundary layer. When the geostrophic regime has a laminar boundary layer flow (at smaller Ra), the viscous dissipation is confined to the thin Ekman layer and the total dissipation integrated over the volume of the Ekman layer scales as $\varepsilon_\nu \sim (\rho_r \nu W L) U^2/\delta_E$. Writing the dissipation in the corresponding non-rotating case (where dissipation is confined to the thermal boundary layer) as $\varepsilon_{0\nu} \sim (\rho_r \nu W L/2) U_{0\nu}^2/\delta_{0\nu}$ and using the geostrophic scaling above, we have

$$\varepsilon_\nu/\varepsilon_{0\nu} = 2c_{7\nu} Q_\nu^{-5/6}, \tag{13}$$

which implies that dissipation is smaller for more rapid rotation (at a fixed Ra). The result also predicts that the effect of a given rotation rate is smaller for stronger buoyancy forcing (ie. larger Q, within the laminar range of Ra). At large Ra, on the other hand, we postulate that the dissipation is dominated by small turbulent scales and spread through the convecting thermal boundary layer, and potentially also into the interior flow. It remains uncertain how these small scales can be affected by rotation, simply because they are turbulent and this makes it very difficult to predict a scaling relation. We do note that it would take a strong rotation rate to influence the very smallest scales in the flow and, even if the dissipation were to be influenced, the upper limit on the maximum total dissipation in the system (ε_{max}) must hold.

For both the laminar and turbulent boundary layer cases, the irreversible mixing relationship with the Nusselt number (6) is expected to hold in the geostrophic regime. This is because the assumptions made to derive this relation do not change with the introduction of rotation. Using (6) with the large Ra turbulent geostrophic scaling (12) for heat flux implies a mixing rate of

$$\Phi_d/\Phi_{d0} = c_8(QPr)^{-1/3}. \tag{14}$$

A similar relation can be derived for the small Ra laminar geostrophic scaling, except with the Pr term removed because (3) and (8) are used instead of (4) and (9). Thus the mixing rate in the geostrophic regime is predicted to decrease with increasing rotation.

Considering the mixing efficiency (7) in the turbulent range of the geostrophic regime, we assume that dissipation is not affected by rotation $\varepsilon \approx \varepsilon_0$ (which is likely true at rotation rates that are not large enough to influence the smallest turbulent scales in the system) and (14), and find

$$\eta \approx 1 - \frac{\varepsilon_0}{c_8(QPr)^{-1/3}\Phi_{d0}}. \tag{15}$$

Hence the mixing efficiency under strong buoyancy forcing is expected to decrease with increasing rotation (which increases Q) but to increase with increasing buoyancy forcing (which both decreases Q and increases the ratio Φ_{d0}/ε_0 of mixing and dissipation rates for the relevant non-rotating case).

Finally, as (6) is expected to hold for the geostrophic case, the definition of the mixing efficiency (7) reduces to (1), on assuming $\varepsilon \approx \varepsilon_{max}$ and dropping prefactors. The prediction is not valid when the dissipation ε is significantly smaller than the upper limit of dissipation ε_{max}, either according to (13) for the laminar case where rotation decreases the dissipation, or potentially when extremely rapid rotation influences the turbulence scales. Dissipation will also decrease, irrespective of Rayleigh number, when $\delta \geq H$, the bottom-to-top temperature difference decreases and extreme rotation shifts the flow into the conductively dominated regime.

3. Methodology

The incompressible, non-hydrostatic Navier-Stokes momentum equation in a rotating coordinate frame and in the Boussinesq approximation with a linear equation of state, along with conservation of mass and heat,

$$Pr^{-1}(\frac{\mathrm{D}\hat{\mathbf{u}}}{\mathrm{D}\hat{t}} + \nabla\hat{p}) = \nabla^2\hat{\mathbf{u}} + Ra\hat{T}\mathbf{k} - E^{-1}\mathbf{k}\times\hat{\mathbf{u}},$$
$$\nabla\cdot\hat{\mathbf{u}} = 0,\ \frac{\mathrm{D}\hat{T}}{\mathrm{D}\hat{t}} = \nabla^2\hat{T}, \tag{16}$$

are solved using direct numerical simulations. Here the hats signify non-dimensionalised values, bold font indicates vectors, the velocity is $\hat{\mathbf{u}} = (u, v, w)$, $\hat{t}$ is time, $\hat{p}$ is the pressure deviation from the hydrostatic, $\hat{T} = (T - T_c)/\Delta T$ is the temperature and $\mathbf{k}$ is the unit upward vector. The variables have been non-dimensionalised by length L, time L^2/κ, mass $\rho_r L^3$ and temperature difference ΔT.

All governing parameters (2) other than the Ekman number are chosen to take the same values as in existing DNS studies of the non-rotating case [*Gayen et al.*, 2013, 2014] and to model laboratory experiments in a rectangular basin [*Mullarney et al.*, 2004; *Stewart et al.*, 2011; *Griffiths et al.*, 2013]. Likewise, all boundary conditions are the same. The basin geometry is defined by aspect ratios $A = 0.16$ and $B = 0.24$. All boundaries are impermeable and non-slip, and all except the base are adiabatic. The temperature applied at the base is a tanh profile in the x direction (the long dimension of the basin) with the gradient confined to within $0.06L$ of the centre point $\hat{x} = 1/2$. Table 1 outlines the simulation conditions: the laminar and turbulent boundary layer regimes are obtained by using two different Rayleigh numbers ($Ra = 7.4 \times 10^8$ and $Ra = 7.4 \times 10^{11}$ respectively), and at each of these the effects of rotation are examined by a range of Ekman numbers. The larger of the Rayleigh numbers is the maximum practical for DNS given computational capacity and the number of solutions required. Prandtl number is $Pr = 5$ for all cases. As usual, the problem is non-dimensionalised in the interests of dynamical interpretation and application of the results to any experimental or oceanic case.

The solution grid for the larger Ra is $768 \times 256 \times 256$ cells, clustered to resolve top and bottom Ekman layers and Stewartson boundary layers on the vertical walls. In an additional run (with the maximum rotation $E = 6.4 \times 10^{-8}$) the grid is $1536 \times 512 \times 512$ cells and confirmed the solution is well resolved. For the smaller Ra the grid is $384 \times 128 \times 128$. The grid resolution $\Delta_{x,y,z}$ was compared to the Batchelor microscale $\eta_b = (\nu^3/\epsilon^*)^{1/4} Pr^{-1/2}$ (where ϵ^* is the local dissipation rate) to ensure the resolution criterion $[\Delta_x, \Delta_y, \Delta_z]_{max} \leq \pi\eta_b$ is satisfied and the smallest scales of motion are accurately resolved everywhere [*Stevens et al.*, 2010; *Gayen et al.*, 2014]. Most importantly, adequate resolution was confirmed by accurate closure of the mechanical energy budget [*Gayen et al.*, 2014].

The solutions were initialised with a uniform water temperature of $\hat{T} = 0.66$, chosen such that a net increase in temperature was required to reach thermal equilibrium, thus facilitating the most rapid equilibration [*Griffiths et al.*, 2013]. Once in thermal equilibrium, simulations were continued for an additional period of 320 and 10 buoyancy timescales $L/(g\alpha\Delta TH)^{1/2}$ for $Ra = 7.4 \times 10^8$ and 7.4×10^{11}, respectively, in order to time average the fluctuating flow.

4. Results

4.1. Dynamics

At the smaller Ra the boundary layer is laminar at all rotation rates. At $Q_\nu = 18$ (Figure 2a) this Ra gives upwelling both in an endwall plume and in the interior above the heated boundary, within quasi-steady, basin-scale horizontal gyres. For extreme rotation ($Q_\nu = 4422$; Figure 2b) the vertical velocities and kinetic energy are trivially small and slow horizontal motion is largely parallel to contours of applied temperature on the base, focused around the large temperature gradient at the centre of the basin, and consistent with the predicted extreme rotation regime in which heat transport is predominantly by conduction [*Hignett et al.*, 1981].

At the larger Ra and $Q = 5.9$ (temperature inset in Figure 1; Figure 2c) the stably stratified thermal boundary layer is laminar over the cooled region of the base but caps a mixed layer of small-scale convection over the heated region, as in the non-rotating case [*Mullarney et al.*, 2004; *Gayen et al.*, 2013]. Rotation does not strongly influence the boundary layer instabilities, which occur near the 'leading edge' of the heated region as two-dimensional rolls (not shown in Figure 2) aligned parallel to the local boundary layer flow velocity and subsequently break up into three-dimensional turbulent convection within the mixed layer. These small scales are largely de-coupled from geostrophic eddies in the interior flow. However, rotation leads to deep upwelling in the interior above the heated boundary, in plumes that are cyclonic vortices of larger scale than the boundary layer instabilities. We refer to these deep convective vortices distant from the side boundaries as 'chimneys' (after *Killworth* [1979]). There is also evidence of basin-scale gyres, with a particularly strong gyre near the mid-point of the domain but slightly offset toward the heated end. At $Q = 147$ (Figure 2d) the chimneys extend coherently through the interior and boundary layer. The chimneys are unsteady features with lifetimes of order 10 rotation periods. The horizontal length scale of the chimneys decreases and there are a greater number present with increasing rotation rate. In time-averaged flow (not shown here) at $Q = 147$ there are signs of basin-scale gyres that are more difficult to discern over the many stronger but short-lived structures in the instantaneous flow.

The result that small-scale instabilities occur in the rotating flow at the larger Ra much as in the non-rotating case implies that turbulent dissipation may be similar and that our hypothesis, that dissipation may be insensitive to rotation, may be correct. In contrast, the absence of small-scale turbulence at the smaller Ra is consistent with laminar dissipation overwhelmingly within the viscous Ekman layer, which suggests that the dissipation in that regime is smaller at larger rotation rates, where the Ekman layer is thinner.

4.2. Boundary layer thickness and heat transport

We define the thermal boundary layer thickness as encompassing 90% of the bottom-to-top temperature difference (horizontally averaged in $\hat{y}$ at $\hat{x} = 0.75$). In Figure 3a the boundary layer thickness has been normalised by the domain length, as suggested by the scaling (10), and plotted against the inverse Ekman number so that the horizontal axis displays increasing rotation rate. The boundary layer is thinner for stronger buoyancy forcing, and it thickens with increasing rotation for both Rayleigh numbers. For the larger Ra the thickening is consistent with the geostrophic scaling (10) once the rotation rate is greater than $1/E > 10^5$. The thickening in δ is also consistent with the previous laboratory measurements [*Park and Whitehead*, 1999] at a slightly smaller Rayleigh number. For the smaller Ra used here, and $1/E > 10^6$ (given the vertical aspect ratio of the domain chosen in this study), the boundary layer thickness approaches the water depth ($H = 0.16L$, noting also that the definition of δ would place it at $0.9H$ for a linear temperature gradient). The strong stratification throughout the depth demonstrates that the conditions are approaching the conduction regime predicted for extremely rapid rotation.

The dimensionless heat transport, or Nusselt number, is calculated as $Nu = (\overline{dT/dz})/(\Delta T/L)$, where $\overline{dT/dz}$ is the vertical temperature gradient at the boundary horizontally averaged over the heated region [*Gayen et al.*, 2014], the latter coinciding exactly with the region of negative temperature gradient and heat input. Figure 3c shows that, at the larger Ra, the computed Nusselt number decreases with increasing rotation in a manner that is again consistent with the geostrophic scaling (10). A similar decrease is not entirely reflected in the earlier laboratory measurements, at least in part because a constant heat flux boundary condition was used in the experiments and this requires a modified definition of the Nusselt number [*Park and Whitehead*, 1999]. Those measurements are therefore shown here for completeness and indicate a reasonable level of consistency allowing for the different boundary conditions. At the smaller Rayleigh number the heat transport is smaller and similarly decreases with increasing rotation rate.

In order to more directly compare the influence of rotation at the different strengths of buoyancy forcing, Figures 3b,d (see also Table 1) show the present DNS results normalised by the non-rotating scaling (3) or (4) established from equivalent DNS for non-rotating flow, and plotted against Q_ν or Q. This normalisation removes the previously established Rayleigh number dependence of the non-rotating flow, revealing both the influence of rotation and any difference in the Rayleigh number dependence in the rotating cases. It also shows the significance of the ratio of rotation effects to buoyancy forcing, as indicated by the ratio of boundary layer thicknesses. At $Q < 1$ (and $Q_\nu < 1$) rotation has negligible effect on either thermal boundary layer thickness or heat transport, independent of Ra. At $1 < Q < 10^2$ (and $1 < Q_\nu < 10^2$) the boundary layer thickens and heat transport decreases with increasing Q (Q_ν) in the manner predicted by the geostrophic scaling (11, 12) (so long as $\delta < H$). Fitting the scaling law to these results for the larger Ra provides estimates of the numerical prefactors ($c_5 = 0.50 \pm 0.01$, $c_6 = 2.4 \pm 0.3$) for the turbulent boundary layer regime. At $Q_\nu > 10^2$ the thermal boundary layer thickness for the smaller Rayleigh number is again seen to approach the water depth and the flow approaches the conduction regime, a transition that occurs at a value of Q (Q_ν) which depends on both Ra and the aspect ratio A. The Nusselt number for the largest Q_ν may appear to support geostrophic scaling ($Nu/Nu_{0\nu} \sim Q_\nu^{-1/3}$). However, both the large boundary layer thickness and the small value of the Nusselt number ($Nu < 2$) belie this interpretation.

The results confirm that the boundary layer flow and heat transport under rotation depend strongly on Q. They also confirm that the separate scaling for laminar and turbulent cases serves to largely collapse the results. However, at $Q_\nu \approx 20$, it can be seen that rotation has a lesser influence for the smaller Ra than it does at the larger Ra, particularly in the Nusselt number. This results from an enduring influence of the viscous term in (16) for the smaller Ra, relative to the buoyancy and Coriolis terms, which shifts the approach to geostrophic balance in the boundary layer flow to somewhat larger Q_ν [*Stern*, 1975; *Hignett et al.*, 1981].

4.3. Dissipation, mixing, and mixing efficiency

Figure 4 shows the computed rates of viscous dissipation ε and irreversible mixing Φ_d normalised by the corresponding non-rotating values (taken from interpolation of the results of *Gayen et al.* [2014]) for each of the two Rayleigh numbers and plotted against Q or Q_ν. The dissipation and mixing rates were computed from the primitive expressions (§2.1), the mixing rate requiring extensive computation of the adiabatic reordering of fluid parcels to their gravitation equilibrium positions at every time step over a lengthy time period and then averaging over time. The production of available potential energy by the boundary heat fluxes ($\kappa g \oint z^*(\partial\rho/\partial x_i)dS$) was also computed at each time step and again averaged over time. There were no significant differences between the mixing rate and surface buoyancy forcing flux, consistent with the non-rotating case, confirming that the energy budget was closed in all cases. The dissipation (Figure 4a) remains unaffected by rotation ($\varepsilon \approx \varepsilon_0$) up to a value of Q that depends on Rayleigh number: indeed for the larger Ra the dissipation remains largely unchanged by rotation in all our solutions. For the smaller Ra it decreases rapidly with Q_ν at $Q_\nu \geq 10^2$. The latter result is consistent with the dissipation scaling for laminar flow (13) and the former is consistent with our hypothesis that rotation does not substantially alter dissipation rates when dissipation is predominantly through small-scale turbulent convection.

The mixing rate (Figure 4b) decreases with increasing rotation rate for sufficiently large Q, and supports the geostrophic scaling (14). For the turbulent case $Ra = 7.4 \times 10^{11}$, the geostrophic regime begins at approximately $Q = 1$ and a fit of the scaling prediction to the three results at $5.9 \leq Q \leq 147$ provides the prefactor $c_8 = 2.7 \pm 0.2$. As noted for the heat transport, the mixing rate shows evidence of a greater influence of viscous stress at moderate Q_ν, which shifts the onset of geostrophic balance to slightly larger Q_ν. The mixing rates are almost identical to the normalised Nusselt numbers (with only a slight vertical shift for different Ra cases), as expected from the similar form of the expressions for surface buoyancy forcing and Nusselt number, and supports the assumption that the relation (6) applies in the geostrophic regime. Thus the reduction of mixing rate by Coriolis effects is in line with the reduction in total heat transport through the system.

Finally the mixing efficiencies (Table 1 and Figure 5a) were calculated directly from (7). In the laminar flow at the smaller Ra the mixing efficiencies decrease with increasing rotation, up to $Q_\nu \approx 200$, owing to a greater reduction in mixing relative to the decrease in dissipation. However, at larger Q_ν the efficiency increases steeply and is close to 100% for the conduction dominated solution at $Q_\nu = 4422$. The minimum in η is expected to occur as the conditions approach the transition from the advection dominated geostrophic regime, in which Coriolis effects control boundary layer flow and decrease heat transport and mixing rate, to the extremely rapid rotation regime under which flow is very slow ($\varepsilon \to 0$), heat transport is by conduction ($Nu \to O(1)$) and $\eta \to 1$ at $Q \to \infty$. The turbulent, large Rayleigh number cases similarly show mixing efficiencies decreasing with increasing rotation, and these are well described by the scaling prediction for the geostrophic regime (15).

The mixing efficiencies for the non-rotating and strongly rotating (geostrophic) regimes, for both laminar and turbulent cases, all collapse reasonably close to the single curve (1) in terms of the heat transport (Figure 5b). Although the flow at the smaller Ra does not fully satisfy the assumptions of the the large Rayleigh number scaling prediction, the mixing efficiency lies close the theoretical scaling (1) for all cases having $NuA > 2$, which relates to a thermal boundary layer thickness much less than the water depth. The minimum in mixing efficiency for the smaller Ra occurs at $NuA \approx 1$. The deviation from the geostrophic scaling at $NuA < 1$ is consistent with the predication that the flow transitions to the conduction regime when $\delta \geq H$. The corresponding transition from geostrophic to conduction regimes for the larger Ra is not practically accessible with DNS.

5. Discussion

Viscous dissipation in horizontal convection in the absence of rotation occurs largely through turbulence if $Ra > 10^{11}$, and is due primarily to small scale convection within the boundary layer for conditions in the range $10^{11} < Ra < 10^{13}$, with shear instability in both the boundary layer and interior becoming more important at $Ra > 10^{14}$ [*Gayen et al.*, 2014]. The geostrophic flows at the two Rayleigh numbers considered here show laminar and turbulent boundary layers in accord with the non-rotating cases. Thus for

$Ra = 7.4 \times 10^{11}$ dissipation occurs predominantly through turbulent convection in the thermal boundary layer. The effects of rotation in the geostrophic regime do not directly influence the relatively small scales of turbulent motion, and dissipation rates can be influenced only through the increase of thermal boundary layer thickness or decrease of boundary layer velocity scale with increasing rotation according to the geostrophic scaling. In the absence of a theoretical scaling for the turbulent dissipation rates, we speculate that the dissipation remains independent of rotation to a first approximation, unless rotation is so rapid that a Rossby number for the turbulence scales is of order one or less, where the turbulent motions will tend to become coherent in the direction of the planetary rotation vector [*Bardina et al.*, 1985; *Jacquin et al.*, 1990]. The conditions at which the turbulent dissipation begins to decrease substantially with further increase of rotation will then give the minimum mixing efficiency. This minimum occurs because, even though the rate of irreversible mixing continues to decrease with increasing rotation and acts to decrease the mixing efficiency throughout, the dramatic reduction in dissipation at extreme rotation comes to dominate the mixing efficiency calculation, causing it to increase once again.

One approximation to find the minimum mixing efficiency is to consider the largest scales of turbulent motions in the boundary layer, of order δ, and evaluate a turbulence Rossby number $Ro_T \sim U/(f\delta) \sim Pr^{-1}RaE^2$ using the geostrophic scaling (10). Rotation will influence boundary layer turbulence at $Ro_T < 1$ (which is in dimensional terms $f > (g\alpha\Delta T/L)^{1/2}$). This condition is exceeded for the larger Ra at the maximum rotation rate examined ($Q = 147$, $Ro_T \approx 6 \times 10^{-4}$), for which the flow solutions already indicate strong vertical coherence of small scale vortical motions and a very small reduction of dissipation rate.

The above criterion may over-estimate the effect of rotation on the dissipation scales of the turbulence, hence under-estimating the value of Q at which the minimum mixing efficiency occurs. A criterion that likely under-estimates the Coriolis effect on turbulent dissipation is the microscale Rossby number $Ro_D \sim u_D/(fl_D) \approx 1$, where $l_D \sim (\nu^3/\varepsilon^*)^{1/4}$ and $u_D \sim (\varepsilon^*\nu)^{1/4}$ are the Kolmogorov length and velocity scales of turbulence based on the dissipation rate per unit mass ε^*. This condition implies that rotation affects the Kolmogorov scale at $f \approx (\varepsilon^*/\nu)^{1/2}$. As most (approximately 80%) of the dissipation remains confined to the boundary layer at the modestly large Ra used here, the volume integrated dissipation rate is $\varepsilon \approx \varepsilon^*\rho_r\delta WL/2$ and the geostrophic scaling (10) gives the Rayleigh number, Ra_m, or Ekman number E_m, at minimum mixing efficiency along with the corresponding Nusselt number, Nu_m:

$$Ra_m \sim k_1 Pr^{3/2} E_m^{-7/4},\ Nu_m \sim k_2 Ra_m^{1/7} Pr^{2/7}, \tag{17}$$

where $k_1 = 0.0048$ and $k_2 = k_1^{4/21} = 0.36$ are merely estimates of upper bounds on the prefactor values, given the observation that dissipation at $Q = 147$ has not significantly decreased from the non-rotating case. The minimum efficiency from (1) is then $\eta_m \approx 1 - 1/(k_2 Ra^{1/7} Pr^{2/7} A)$, from which we see that $\eta_m \to 1$ for $Ra^{1/7}Pr^{2/7}A \gg 1$. For $Ra = 7.4 \times 10^{11}$, we find $ANu_m \approx 4.5$ and $\eta_m \approx 0.78$, values that are consistent with the DNS results; however this is unsurprising as the scaling was fitted to this strong rotation case. At rotation rates larger than that at the locus (17) of $\eta = \eta_m$ for a given buoyancy forcing, the decreasing dissipation in (7) increases η with increasing rotation rate and in the limit of extremely rapid rotation $\eta \to 1$.

For the smaller buoyancy forcing, $Ra = 7.4 \times 10^8$, the minimum mixing efficiency given by the DNS is $\eta = 0.51$ at $Q_\nu = 177$ (Table 1). A smaller efficiency, $\eta = 0.17$, was reported for $Ra \approx 10^8$ in a rotating re-entrant channel model [*Barkan et al.*, 2013] but this is in part due to an *increase* in the reported viscous dissipation, by almost a factor of two, with the introduction of rotation. However, both our simulations and the scaling (13) indicate a decrease in dissipation with rotation for circulation in a closed domain. It is unknown whether the larger dissipation results from the periodic boundary conditions at the ends of their channel (which removes side wall boundary currents) or the parameterised boundary friction used in that study.

A regime diagram (Figure 6) serves to summarise the dominant flow dynamics and predictions for the mixing efficiency. The dynamical regimes indicated are based largely on the results (discussed in §2) of *Hignett et al.* [1981] for rotating circulation and *Gayen et al.* [2014] for the non-rotating case. Also indicated are the conditions for the present simulations and previous studies having a vertical aspect ratio A close to the present study (and $Pr \approx 5$). As the transition to the conduction regime lies at larger Ra for smaller A, the inner frame of the diagram shows the predicted regime boundaries for $A = 0.16$ and the outer section shows the transitions for the aspect ratio of an ocean basin (see §6). Contours of mixing efficiency in the non-rotating and weakly rotating regime are taken from the non-rotating DNS results for laminar and turbulent cases [*Gayen et al.*, 2014], extrapolated to join contours in the geostrophic regime at $Q > 1$ given by (15), recalling that both non-rotating and geostrophic contours involve prefactors obtained from the DNS results. The diagram illustrates the asymptotic behaviour, $\eta \approx 1$, at very strong buoyancy forcing irrespective of rotation rate, and a trough (dashed line) of reduced mixing efficiency within the geostrophic regime. The reduction of efficiency in the trough becomes less significant for stronger buoyancy forcing. The mixing efficiency at conditions to the right of the trough are unknown apart from the prediction that $\eta \to 1$ in the conduction regime. The only previous examination of the mechanical energy budget with rotation (but for a re-entrant channel) [*Barkan et al.*, 2013] lies in the laminar geostrophic regime at conditions where the present results predict $\eta \approx 0.7$.

6. Ocean application

In order to relate the results to the ocean it is necessary to evaluate A, Pr, Ra and E. The variables $f \approx 4 \times 10^{-5}\,\mathrm{rads}^{-1}$, $g = 10\,\mathrm{ms}^{-2}$, $L \approx 6 \times 10^{6}\,\mathrm{m}$, $W \approx 5 \times 10^{6}\,\mathrm{m}$ (total surface area 3×10^{13} m^2) and $\Delta T \approx 30°\mathrm{C}$ are straightforward. The coefficient for thermal expansion relevant to an ocean basin that extends to high latitude sinking regions, such as in the North Atlantic, is $\alpha \approx 5 \times 10^{-5}$, noting that the density differences important to both surface mixed layer convection and to deep, large scale circulation are those at temperatures in the regions of destabilising surface cooling and deep sinking [*Hughes et al.*, 2007]. The relevant kinematic viscosity and buoyancy diffusivity are those governing friction and heat transport in the surface Ekman and thermal boundary layers. Previous analyses of the surface Ekman layer give a turbulent viscosity $\nu = O(10^{-2})\,\mathrm{m}^2\mathrm{s}^{-1}$ [*Price et al.*, 1987; *Chereskin*, 1995; *Schudlich and Price*, 1998], from which $E = O(10^{-11})$ and Ekman layer thickness $\delta_E \approx 20\,\mathrm{m}$.

It is important that the near-surface ocean turbulence is largely energised by wind, an independent energy input, and the parameters E and Ra must be evaluated on a consistent basis. We therefore consider that the small-scale wind driven turbulence sets not only the effective viscosity for the Ekman layer, but also the diffusivity for buoyancy. Molecular values play no significant role in determining the transport of momentum and heat within the water column. However, the Ekman layer diffusivity (taking $Pr \approx 1$) and the geostrophic scaling (10) would give a thermal boundary layer thickness $\delta > 2000\,\mathrm{m}$, which is too large to allow an assumption that the surface diffusivity applies through the entire boundary layer thickness. Estimates from ocean data at $100-400\,\mathrm{m}$ depth indicate diapycnal diffusivities in the ocean pycnocline not much greater than $10^{-5}\,\mathrm{m^2s^{-1}}$ [*Kunze and Toole*, 1997; *Ledwell et al.*, 1998]. However, use of such a small diapycnal diffusivity in the present scaling would predict a thermal boundary layer thickness $\delta \sim 20\,\mathrm{m}$, which is less than both the Ekman layer thickness and average sub-tropical mixed layer depth above which we expect large diffusivities, and is therefore invalid as a value for the thermal boundary layer. An effective average diffusivity for the boundary layer is therefore difficult to define. However, the small inferred diffusivity in the ocean pycnocline implies that the boundary layer thickness predicted by the scaling is likely to be limited to slightly more than the mixed layer depth, hence greater than order 50 m. Average boundary layer diffusivities consistent with this observation are at least 10^{-4} $\mathrm{m^2s^{-1}}$ or (less likely) 10^{-3} $\mathrm{m^2s^{-1}}$. With $Pr \approx 1$ these values give $Ra \sim 10^{26}$ and 10^{24}, and the geostrophic scaling (11) then gives $\delta \sim 80\,\mathrm{m}$ and $360\,\mathrm{m}$, respectively. An ocean depth of 5000 m gives aspect ratio $A \approx 8 \times 10^{-4}$. These ocean conditions are indicated by the bar on Figure 6, where the outer region shows the predicted regime transitions for and ocean basin with $A = 10^{-3}$.

Notwithstanding the strong buoyancy forcing implied by the very large Rayleigh number, the values above place the ocean in the 'strong rotation' regime (from (9) $Q \approx 4-22$). The geostrophic scalings (12,14) with (4) predict $Nu \approx (3-12) \times 10^4$ and total irreversible mixing rate $\Phi_d \approx (2-4) \times 10^{12}\,\mathrm{W}$ (assuming $\varepsilon \approx \varepsilon_0$). For a comparison, an independent estimate of Nu can be found from previous estimates of meridional heat transport (1 PW) in the Atlantic from ocean data [*Hall and Bryden*, 1981; *Houghton et al.*, 1996; *Macdonald* *and Wunsch*, 1996; *Ganachaud and Wunsch*, 2000]. The value corresponds to an average flux $F \approx 70\,\mathrm{W\,m^{-2}}$ through the cooling area of the surface, which is half the surface area of the basin. It can be shown from the nature of the mixing term Φ_d in the mechanical energy budget that this approach to evaluating Nu must be based on a volume averaged diffusivity. Using $\kappa = 10^{-4}\,\mathrm{m^2s^{-1}}$, $\rho_r = 10^3\,\mathrm{kgm^{-3}}$, and $c_p = 4 \times 10^3\,\mathrm{Jkg^{-1}K^{-1}}$, we again find $Nu = FL/(\rho_r c\kappa\Delta T) \approx 3 \times 10^4$. The mixing efficiency (1) becomes $\eta \approx 0.95 - 0.99$, and we emphasise that this describes the total rate of mixing relative to the total mechanical energy supplied to the ocean by the surface buoyancy forcing. Thus it does not include the dissipation of kinetic energy derived from other forcing.

The value $\eta \geq 0.95$ indicates that the ocean buoyancy forcing is efficient at driving mixing, which in turn means that heat can be transported through the system with minimal dissipation of the mechanical energy input from buoyancy fluxes. In addition to the energy considerations, the simulations in the geostrophic regime show a boundary layer structure, a convective mixed layer, 'open ocean' convection in the form of small-scale convection chimneys, a field of mesoscale baroclinic eddies, and basin-scale mean gyre circulation, all somewhat similar to oceanic features. In the simulations all of these features result from buoyancy forcing alone. The large-scale gyres are of particular note for future study, as the mid-latitude oceanic gyres are generally considered to be predominantly driven by wind stress, despite buoyancy playing a crucial role in the geostrophic scaling for the large-scale circulation. The convection associated with buoyancy forcing, manifest at scales from those in the mixed layer to the global overturning, services to maintain the stratification and the results here support the view that it also plays a key role in the energy budget.

7. Conclusions

Simulations of buoyancy-driven circulation in a rectangular basin confirm that rotation decouples the viscous and thermal boundary layers. Increasing rotation confines viscous flow to a thinner Ekman layer, leaving the thermal boundary layer governed by geostrophic balance, which inhibits mean flow in the direction of the mean temperature gradient excepting in sidewall boundary currents. The thermal boundary layer thickness is then increased, hence decreasing the total heat transport across the boundary layer and into the interior. The simulations are consistent with the geostrophic scaling $Nu/Nu_0 \sim (QPr)^{-1/3}$. The rate of irreversible mixing, closely related to the heat transport, similarly decreases with increasing rotation in the geostrophic regime.

In contrast to the mixing rate, viscous dissipation is controlled by the small scales of flow. Under strong buoyancy forcing ($Ra > 10^{11}$), dissipation is dominated by small scale turbulence. For conditions practical for current DNS, this turbulence is predominantly produced convectively and largely confined to the thermal boundary layer (rather than by shear production which is increasingly distributed through the flow at still larger Ra). The turbulent dissipation in this regime is unaffected by rotation. As a result the mixing efficiency in the geostrophic regime is reduced by rotation solely due to the reduced heat transport and mixing, and is consistent with the theoretical prediction (1) that also applies to non-rotating convection. However, very rapid rotation pushes the flow into a conductive regime having much smaller dissipation and larger mixing efficiency. The smallest possible mixing efficiency is maintained close to 100%, irrespective of rotation rate, by very strong buoyancy forcing.

Extrapolation of the results to circulation in an idealised ocean basin suggests that the ratio of the total irreversible mixing rate to the input of available potential energy supply by surface buoyancy forcing is $\eta \geq 0.95$. Hence less than 5% of the mechanical energy supply from buoyancy is lost to viscous dissipation. The high efficiency implies that convection has a greater chance of influencing circulation in an ocean with multiple sources of mechanical energy, including wind and tides. In this first study we have not included contributions from surface wind stress, which may increase heat transport, or the variation of Coriolis parameter with latitude and steering of the geostrophic flow by bottom topography. However, the Nusselt number obtained independently from the measured ocean heat transport lends support to the high mixing efficiency, and the unaccounted effects are unlikely to significantly alter our conclusions. Sources of turbulent kinetic energy other than buoyancy add to, and likely dominate, viscous dissipation in the oceans but do not change the relation between total mixing rate and boundary buoyancy forcing. Nevertheless, wind-induced Ekman pumping along with strong coupling between the input of available potential energy by surface buoyancy fluxes and the work done by wind stress imply that further examination of the energy sinks under combined wind and buoyancy forcing is required. The principles discussed here could also be useful for understanding turbulent Rayleigh-Bénard convection in the earth's outer core [*Kageyama et al.*, 2008; *King et al.*, 2009; *Hulot et al.*, 2010], where the mechanical energy budget in the geostrophic regime may have implications for the maintenance of the earth's magnetic field.

Acknowledgments. The research was supported by Australian Research Council grant DP140103706 and BG was funded by an Australian Research Council Discovery Early Career Fellowship DE140100089. Numerical computations were carried out on the Australian National Computational Infrastructure, ANU. Model output can be obtained through a written request to the corresponding author (email: Catherine.Vreugdenhil@anu.edu.au). We thank Dr A. McC. Hogg for providing helpful comments and feedback on an earlier version of this paper.

References

Bardina, J., J. H. Ferziger, and R. S. Rogallo (1985), Effect of rotation on isotropic turbulence: computation and modelling, *J. Fluid Mech.*, *154*, 321–336.

Barkan, R., K. B. Winters, and L. Smith (2013), Rotating horizontal convection, *J. Fluid Mech.*, *723*, 556–586.

Bryan, F. (1987), Parameter sensitivity of primitive equation ocean general circulation models, *J. Phys. Oceanogr.*, *17*, 970–985.

Chereskin, T. K. (1995), Direct evidence for an Ekman balance in the California Current, *Geophys. Res. Lett.*, *100*, 18,261–18,269.

Dewar, W. K., P. Berloff, and A.M. Hogg (2011), Submesoscale generation by boundaries, *J. Mar. Res.*, *69*, 501–522, doi:10.1357/002224011799849345.

Ferrari, R., and C. Wunsch (2009), Ocean Circulation Kinetic Energy: Reservoirs, Sources, and Sinks, *J. Fluid Mech.*, *41*, 253–282.

Ganachaud , A., and C. Wunsch (2000), Improved estimates of global ocean circulation,heat transport and mixing from hydrographic data, *Nature*, *408*, 453–457.

Gayen, B., R. W. Griffiths, G. O. Hughes, and J. A. Saenz (2013), Energetics of horizontal convection, *J. Fluid Mech.*, *716*, R10, doi:10.1017/jfm.2012.592.

Gayen, B., R. W. Griffiths, and G. O. Hughes (2014), Stability transitions and turbulence in horizontal convection, *J. Fluid Mech.*, *751*, 698–724.

Griffiths, R. W., G. O. Hughes, and B. Gayen (2013), Horizontal convection dynamics: insights from transient adjustment, *J. Fluid Mech.*, *726*, 559–595, doi: 10.1017/jfm.2013.244.

Hall, M. M., and H. L. Bryden (1981), Direct estimates and mechanisms of ocean heat transport, *Deep-Sea Research*, *29 (3)*, 339–359.

Hignett, P., A. Ibbetson, and P. D. Killworth (1981), On rotating thermal convection driven by non-uniform heating from below, *J. Fluid Mech.*, *109*, 161–187.

Houghton, J.T., L.G. Meira Filho, B.A. Callander, N. Harris, A. Kattenberg, and K. Maskell (1996), *Climate Change 1995: The Science of Climate Change*, Cambridge University Press, Cambridge, England.

Hughes, G. O., R. W. Griffiths, J. C. Mullarney, and W. H. Peterson (2007), A theoretical model for horizontal convection at high Rayleigh number, *J. Fluid Mech.*, *581*, 251–276, doi:10.1017/S0022112004000485.

Hughes, G. O., A. M. Hogg, and R. W. Griffiths (2009), Available potential energy and irreversible mixing in the meridional overturning circulation, *J. Phys. Oceanogr.*, *39*(12), 3130–3146, doi:10.1175/2009JPO4162.1.

Hulot, G., F. Lhuillier, and J. Aubert (2010), Earth's dynamo limit of predictability, *Geophys. Res. Lett.*, *37*, L06305.

Hussam, W. K., T. K. Tsai, and G. J. Sheard (2014), The effect of rotation on radial horizontal convection and Nusselt number scaling in a cylindrical container, *Int. J. Heat Mass Trans.*, *77*, 46–49.

Jacquin, L., O. Leughter, C. Cambon, and M. Mathieu (1990), Homogeneous turbulence in the presence of rotation, *J. Fluid Mech.*, *220*, 1–52.

Kageyama, A., T. Miyagoshi, and T. Sato (2008), Formation of current coils in geodynamo simulations, *Nature*, *454*, 1106–1109.

King, E. M., S. Stellmach, J. Noir, U. Hansen, and J. M. Aurnou (2009), Boundary layer control of rotating convection systems, *Nature*, *457*(7227), 301–304.

Killworth, P. D. (1979), On "Chimney" Formations in the Ocean, *J. Phys. Oceanogr.*, *9*, 531–554.

Kuhlbrodt, T., A. Griesel, M. Montoya, A. Levermann, M. Hofmann, and S. Rahmstorf (2007), On the driving processes of the Atlantic meridional overturning circulation, *Rev. Geophys.*, *45*, RG2001, doi:10.1029/2004RG000166.

Kunze, E., and J. M. Toole (1997), Tidally Driven Vorticity, Diurnal Shear, and Turbulence atop Fieberling Seamount, *J. Phys. Oceanogr.*, *27*, 2663–2693.

Ledwell, J. R., A. J. Watson, and C. S. Law (1998), Mixing of a tracer in the pycnocline, *J. Geophys. Res.*, *103*, 21,499–21,529.

Macdonald, A. M., and C. Wunsch (1996), An estimate of global ocean circulation and heat fluxes, *Nature*, *382*, 436–439.

Marshall, J., and K. Speer (2012), Closure of the meridional overturning circulation through southern ocean upwelling, *Nature Geoscience*, *5*, 171–180, doi:10.1038/NGEO1391.

Morrison, A. K., A. M. Hogg, and M. L. Ward (2011), Sensitivity of the Southern Ocean overturning circulation to surface buoyancy forcing, *Geophys. Res. Lett.*, *38*, L14602, doi:10.1029/2011GL048031.

Morrison, A. K., M. H. England, and A. M. Hogg (2015), Response of Southern Ocean Convection and Abyssal Overturning to Surface Buoyancy Perturbations, *J. Clim.*, *28*, 4263–4278, doi:10.1175/JCLI-D-14-00110.1.

Mullarney, J. C., R. W. Griffiths, and G. O. Hughes (2004), Convection driven by differential heating at a horizontal boundary, *J. Fluid Mech.*, *516*, 181–209, doi: 10.1017/S0022112004000485.

Nikurashin, M., and R. Ferrari (2011), Global energy conversion rate from geostrophic flows into internal lee waves in the deep ocean, *Geophys. Res. Lett.*, *38*, L08610, doi: 10.1029/2011GL046576.

Nikurashin, M., G. K. Vallis, and A. Adcroft (2013), Routes to energy dissipation for geostrophic flows in the Southern Ocean, *Nature Geoscience*, *6*, 48–51.

Nycander, J., J. Nilsson, K. Döös, and G. Broström (2007), Thermodynamic Analysis of Ocean Circulation, *J. Phys. Oceanogr.*, *37*, 2038–2052.

Paparella, F., and W. R. Young (2002), Horizontal convection is non-turbulent, *J. Fluid Mech.*, *466*, 205–214.

Park, Y. G., and J. A. Whitehead (1999), Rotating Convection Driven by Differential Bottom Heating, *J. Phys. Oceanogr.*, *29*, 1208–1220.

Park, Y. G., and K. Bryan (2000), Comparison of Thermally Driven Circulations from a Depth-Coordinate Model and an Isopycnal-Layer Model. Part I: Scaling-Law Sensitivity to Vertical Diffusivity, *J. Phys. Oceanogr.*, *30*, 590–605.

Peltier, W. R., and C. P. Caulfield (2003), Mixing efficiency in stratified shear flows, *Annu. Rev. Fluid Mech.*, *15*, 135–167.

Price, J. F., R. A. Weller, and R. R. Schudlich (1987), Wind-Driven Ocean Currents and Ekman Transports, *Science*, *238*, 1534–1538.

Robinson, A. (1960), The general thermal circulation in equatorial regions, *Deep-Sea Res.*, *6*, 311–317.

Robinson, A., and H. Stommel (1959), The Oceanic Thermocline and the Associated Thermohaline Circulation, *Tellus*, *11*, 295–308.

Rossby, H. T. (1965), On thermal convection driven by non-uniform heating from below: an experimental study, *Deep-Sea Res.*, *12*, 9–16.

Rossby, H. T. (1998), Numerical experiments with a fluid non-uniformly heated from below, *Tellus A*, *50*, 242–257.

Saenz, J. A., A. M. Hogg, G. O. Hughes, and R. W. Griffiths (2012), Mechanical power input from buoyancy and wind to the circulation in an ocean model, *Geophys. Res. Lett.*, *39*, L13605.

Schudlich, R. R., and J. F. Price (1998), Observations of Seasonal Variation in the Ekman Layer, *J. Phys. Oceanogr.*, *28*, 1187–1204.

Scotti, A., and B. White (2011), Is horizontal convection really non-turbulent?, *Geophys. Res. Lett.*, *38*, L21609.

Scotti, A., and B. White (2014), Diagnosing mixing in stratified turbulent flows with a locally defined available potential energy, *J. Fluid Mech.*, *740*, 114–135.

Sheard, G. J., W. K. Hussam, and T. Tsai (2016), Linear stability and energetics of rotating radial horizontal convection, *J. Fluid Mech.*, *795*, 1–35.

Stern, M. E. (1975), Ocean Circulation Physics, International Geophysics series, vol. 19, Academic.

Stevens, R. J. A. M., R. Verzicco, and D. Lohse (2010), Radial boundary layer structure and Nusselt number in Rayleigh-Bénard convection, *J. Fluid Mech.*, *643*, 495–507.

Stewart, K., G. O. Hughes, and R. W. Griffiths (2011), When do marginal seas and topographic sills modify the ocean density structure?, *J. Geophys. Res.*, *116*, doi: 10.1029/2011JC006980.

Tailleux, R. (2009), On the energetics of stratified turbulent mixing, irreversible thermodynamics, Boussinesq models and the ocean heat engine controversy, *J. Fluid Mech.*, *173*, 431–471.

Winters, K. B., P. N. Lombard, J. J. Riley, and E. S. D'Asaro (1995), Available potential energy and mixing in density-stratified fluids, *J. Fluid Mech.*, *289*, 115–128.

Winton, M. (1996), The role of horizontal boundaries in parameter sensitivity and decadal-scale variability of coarse-resolution ocean general circulation models, *J. Phys. Oceanogr.*, *26*, 289–304.

Wunsch C., and R. Ferrari (2004), Vertical Mixing, Energy, and the General Circulation of the Oceans, *Annu. Rev. Fluid Mech.*, *36*, 281–314.

Zemskova, V. E., B. L. White, and A. Scotti (2015), Available Potential Energy and the General Circulation: Partitioning Wind, Buoyancy Forcing, and Diapycnal Mixing, *J. Phys. Oceanogr.*, *45*, 1510–1531.

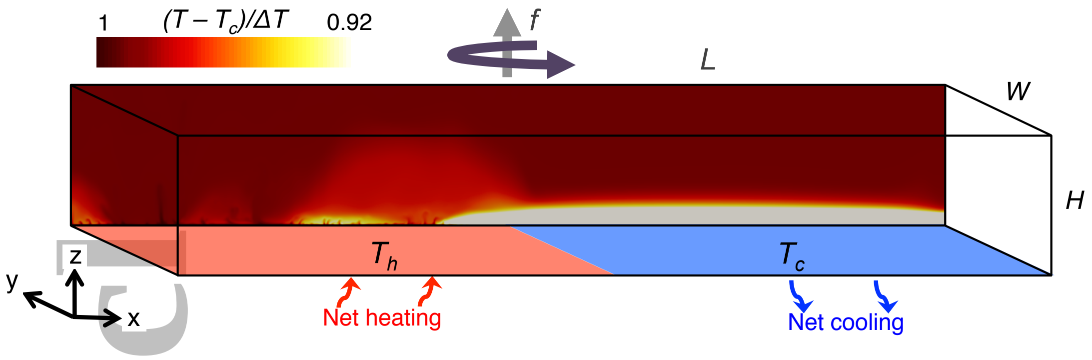

Figure 1. Geometry of DNS set-up with buoyancy forcing at the base. Inset temperature field from the $Ra = 7.4 \times 10^{11}, Q = 5.9$ case taken at $y/W = 0.5$. The highly stratified thermal boundary layer is present over the cooled region.

Table 1. Conditions for DNS and the computed values of boundary layer thickness, Nusselt number and mixing efficiency. The Rayleigh number is varied by changing $g\alpha\Delta T$ (which changes the buoyancy) and the Ekman number is varied by changing the Coriolis parameter f.

Ra	E	Q, Q_ν	δ/δ_0	Nu/Nu_0	η
7.4×10^{11}	1.6×10^{-5}	0.59	0.97	0.926	0.94
7.4×10^{11}	1.6×10^{-6}	5.9	1.51	0.715	0.91
7.4×10^{11}	4.0×10^{-7}	23	2.39	0.553	0.88
7.4×10^{11}	6.4×10^{-8}	147	4.54	0.286	0.78
7.4×10^{8}	1.6×10^{-5}	18	1.76	0.810	0.64
7.4×10^{8}	1.6×10^{-6}	177	2.58	0.277	0.51
7.4×10^{8}	6.4×10^{-8}	4422	2.74	0.086	0.97

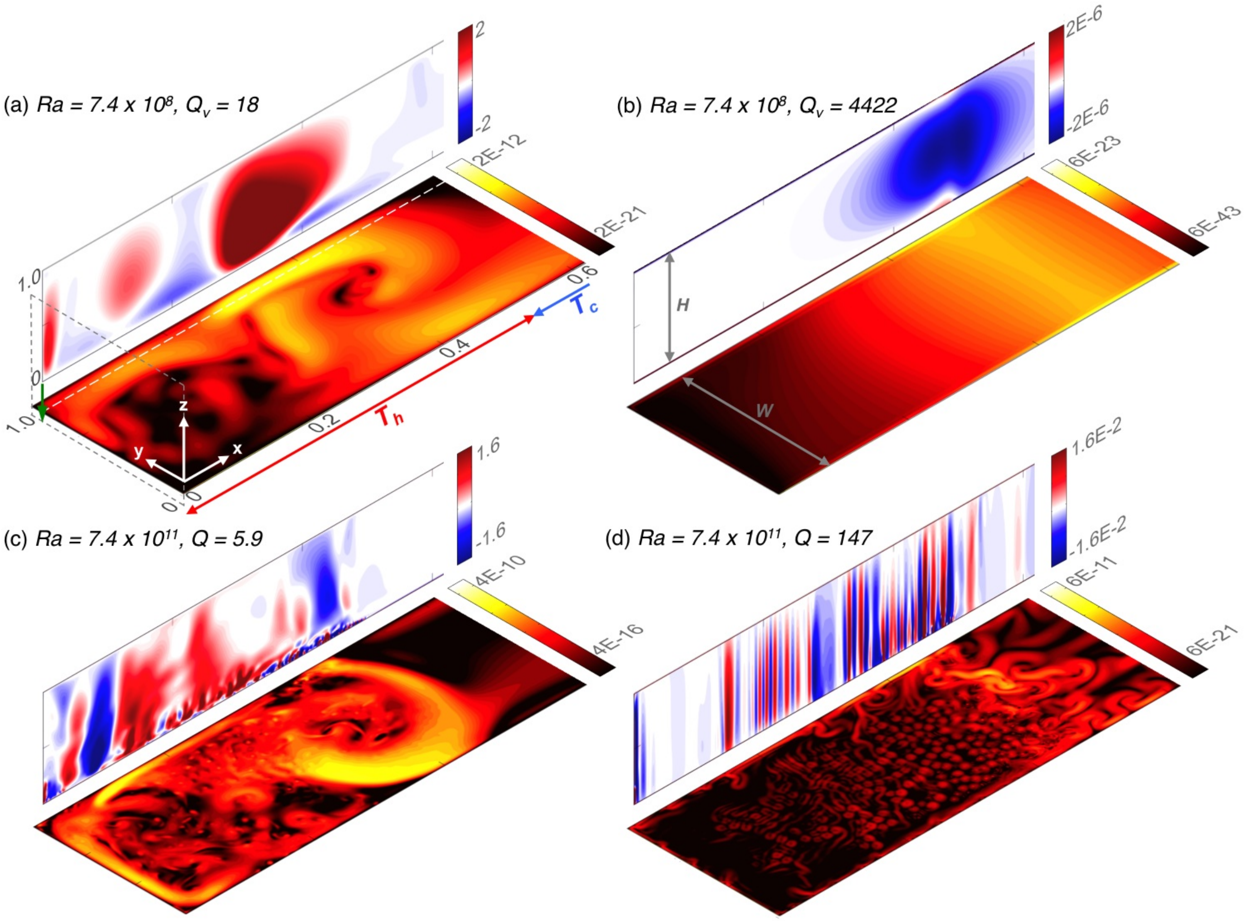

Figure 2. Snapshots of DNS solutions, shown for $0 < \hat{x} < 0.6$: (a) $Ra = 7.4 \times 10^8, Q_\nu = 18$, (b) $Ra = 7.4 \times 10^8, Q_\nu = 4422$, (c) $Ra = 7.4 \times 10^{11}, Q = 5.9$, (d) $Ra = 7.4 \times 10^{11}, Q = 147$. Vertical panels show vertical velocity w normalised by fL (upwards in red, downwards in blue) on the plane $y/W = 0.91$; location of the plane is shown by the green arrow and white broken line at the base in (a). Horizontal planes show kinetic energy $0.5(\mathbf{u}/fL)^2$ (on a logarithmic scale) on the plane $z/H = 0.075$, which is within the thermal boundary layer in all cases. Most kinetic energy is found above the heated region of the base with little of interest above the cooled region. Gravity is directed downwards through the horizontal plane, rotation is anticlockwise and solutions shown are in the large-time thermal equilibrium state.

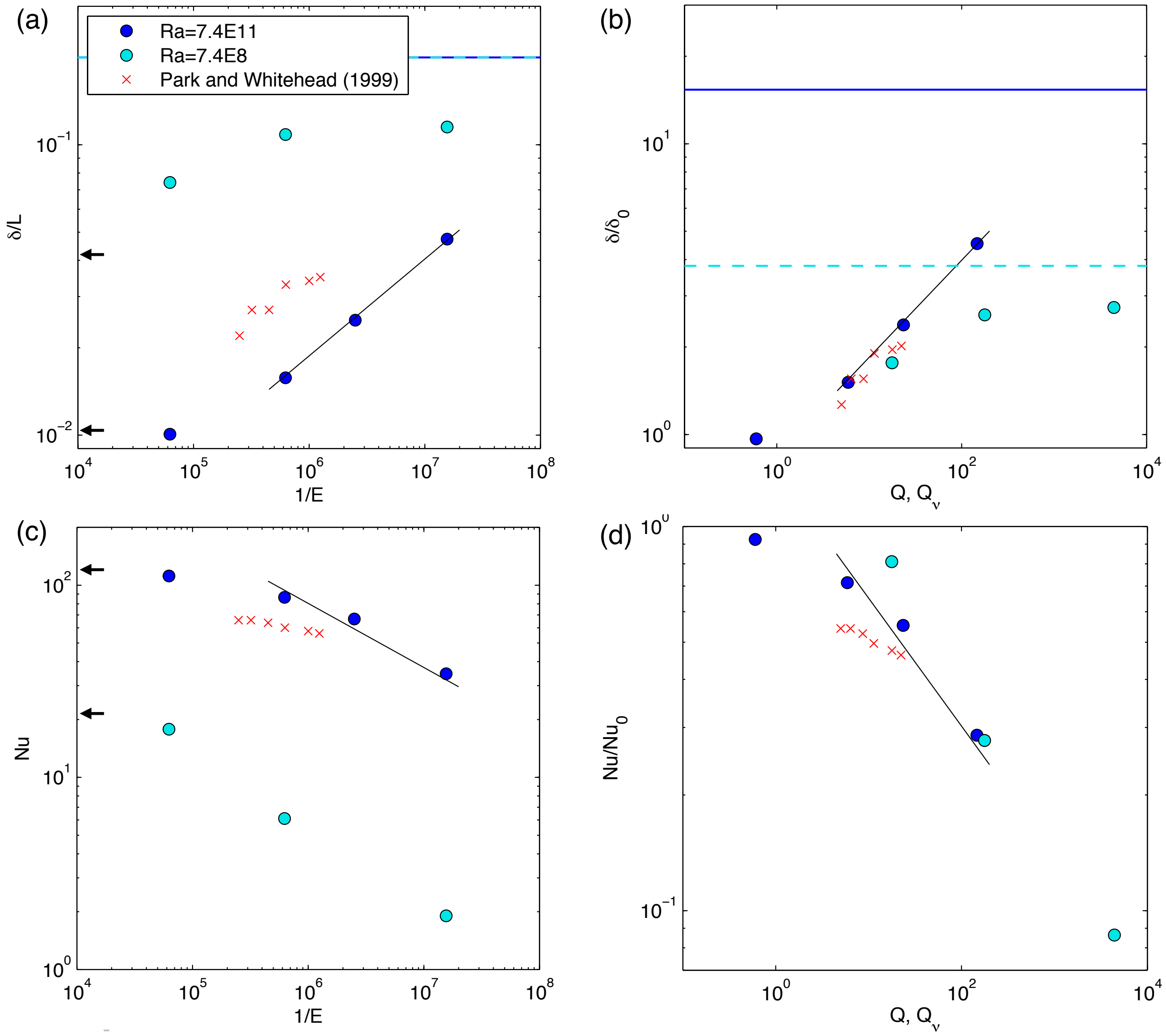

Figure 3. The DNS results for (a) thermal boundary layer thickness δ and (c) Nusselt number Nu as functions of inverse Ekman number. These results are also expressed in (b) and (d) plotted against Q, which serves as a measure of rotation rate. The values are normalised by the corresponding non-rotating values obtained from (3) and (4); these non-rotating values are also indicated by the arrows in (a) and (c). Measurements of *Park and Whitehead* [1999] are shown, but are for a fixed heat flux boundary condition, and are normalised by scaling for the non-rotating inertial regime with applied flux and prefactors from *Mullarney et al.* [2004]. In (a) the horizontal lines indicate the normalised fluid depth H/L and in (b) the normalised fluid depth is H/δ_0 for each Ra (solid line for the larger Ra). Solid lines indicate the geostrophic scaling predictions (11) and (12) fitted to the DNS results for $Ra = 7.4 \times 10^{11}$ with prefactors $c_5 = 0.50 \pm 0.01$ and $c_6 = 2.4 \pm 0.3$.

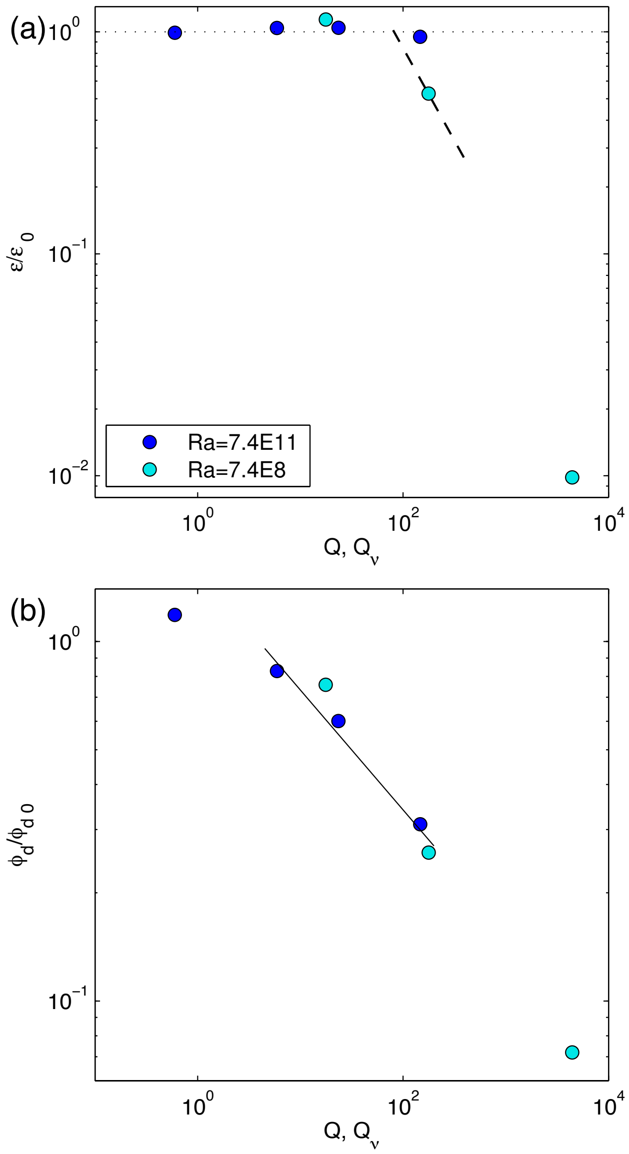

Figure 4. The DNS results for (a) dissipation rate ε and (b) mixing rate Φ_d as functions of Q, a measure of rotation rate. In (a) the non-rotating dissipation ε_0 is calculated using (5) with $c_3 = 0.75$ for the smaller Ra case and $c_3 = 0.93$ for the larger Ra case, based on the results in *Gayen et al.* [2014]. The horizontal dotted line in (a) indicates values equal to the non-rotating result. The broken line shows the dissipation scaling (13) for smaller Ra (matched to the case $Q_\nu = 177$ to find $c_{7\nu} = 20$). In (b) the solid line shows the geostrophic scaling prediction (14) fitted to the results for $Ra = 7.4 \times 10^{11}$ to find $c_8 = 2.7 \pm 0.2$.

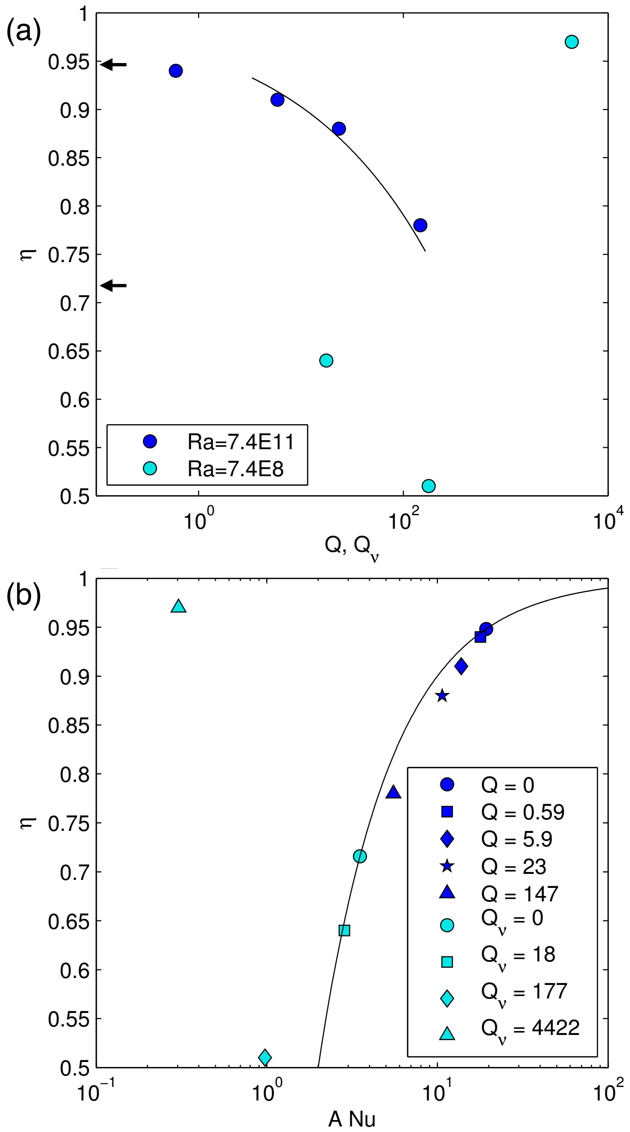

Figure 5. The DNS results for mixing efficiency as a function of (a) the Q parameter and (b) the Nusselt number (multiplied by aspect ratio). In (a) the arrows show the non-rotating values corresponding to each Ra, and the curve is the geostrophic scaling prediction (15) shown for large Ra with $c_8 = 2.7 \pm 0.2$ (from Figure 4b). In (b) symbols indicate the solution keyed to Q and Q_ν, where $Q = 0$ and $Q_\nu = 0$ are the non-rotating cases for each Ra, and the curve shows the theoretical prediction (1) for large Ra.

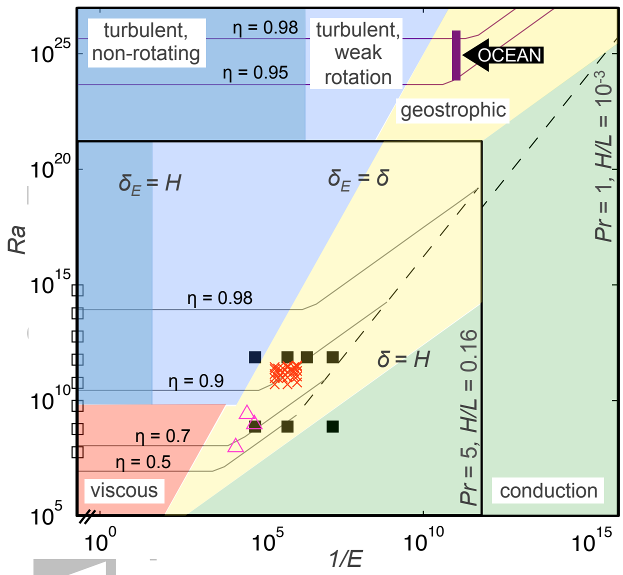

Figure 6. Regime diagram for rotating horizontal convection for $A = 0.16$, $Pr \approx 5$ (inner frame) and $A = 10^{-3}$, $Pr \approx 1$ (outer region), showing that the relative roles of rotation and convection are important. Transitions are described in the text. Contours of mixing efficiency η are from (1) and (4) (non-rotating) and (1) and (12) (geostrophic); broken line shows the approximate location (17) of the bottom of a trough of smaller η within the geostrophic regime. Efficiency $\eta \to 1$ at very large Ra and in the conduction regime. Included are the conditions for the present DNS (solid squares) and previous non-rotating DNS for the same geometry (open squares; *Gayen et al.* [2014]), laboratory experiments of *Park and Whitehead* [1999] for $A = 0.12$ (x) and DNS of *Barkan et al.* [2013] for $A = 0.125$ and 0.25 (triangles). Estimated ocean conditions are shown (purple bar, indicated by arrow).